


(MGS)²-Net: Unifying Micro-Geometric Scale and Macro-Geometric Structure for Cross-View Geo-Localization

Minglei Li¹ , Mengfan He¹, Chunyu Li¹, Chao Chen¹, Xingyu Shao¹, and Ziyang Meng¹

Department of Precision Instrument, Tsinghua University, Beijing 100084, China
liminglei25@mails.tsinghua.edu.cn

Abstract. In this paper, we propose (MGS)²-Net, a geometry-grounded framework that introduces an effective Macro-Geometric Structure Filtering (MGS-F) module to cross-view geo-localization (CVGL). Unlike pixel-wise matching that is commonly used, MGS-F leverages dilated geometric gradients to physically filter out high-frequency facade interferences while emphasizing the view-invariant features on the horizontal plane, directly addressing the oblique-orthogonal view difference. To address the severe scale variations caused by varying UAV flight altitudes, we explicitly incorporate another Micro-Geometric Scale Adaptation (MGS-A) module. MGS-A dynamically utilizes depth priors to rectify scale discrepancies via multi-branch feature fusion. Furthermore, a Structure-Guided Contrastive (SGC) loss is designed to strictly discriminate against cross-view blind spots. Extensive experiments demonstrate that (MGS)²-Net achieves state-of-the-art performance, achieving a Recall@1 of 97.60% on the University-1652 dataset and 98.45% on the SUES-200 dataset. Furthermore, the framework exhibits superior cross-dataset generalization against geometric ambiguity.

Keywords: Cross-View Geo-Localization · Unmanned Aerial Vehicles · Geometric Filtering · Scale Adaptation

1 Introduction

Unmanned Aerial Vehicles (UAVs) have broad applications from urban monitoring to autonomous delivery [1], [2], [3], and achieving robust localization is critical for autonomous flight of UAVs. Since Global Navigation Satellite Systems (GNSS) are often degraded due to signal jamming and multipath effects in complex urban environments [4], Cross-View Geo-Localization (CVGL), matching real-time onboard views against satellite orthophotos, has emerged as an alternative solution [5] [6].

CVGL is challenged by extreme domain shifts: UAV views contain rich multi-perspective imagery, while satellite views are strictly orthographic [7]. To bridge this gap, the current trend is to transfer from CNN-based metric learning [8], [9] to Vision Transformer (ViT) approaches like TransGeo [10], and L2LTR [11].

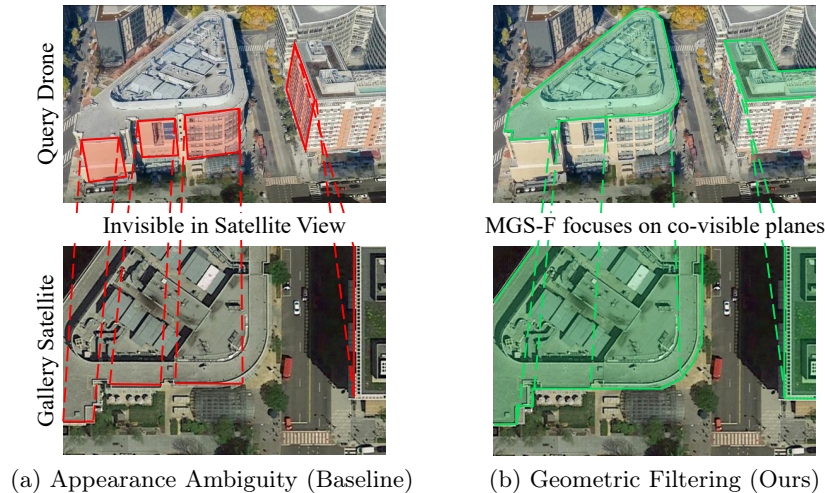


Fig. 1: From Texture Dependency to Geometric Grounding. (a) Visual Ambiguity: Existing methods often overfit to view-dependent vertical facades (red boxes) that are invisible in the satellite orthophoto, leading to retrieval failure. (b) Our Solution: MGS-Net filters out these vertical interferences via MGS-F and robustly focuses on view-invariant rooftops (green boxes), ensuring consistent cross-view alignment.

Recent works have further refined feature granularity through content-aware hierarchical representation selection [12] and correlation-aware learning [13].

Despite these advancements, existing methods lack explicit 3D structural awareness. In dense urban scenarios, the primary bottleneck is macro-level structural noise: oblique UAV images feature a greater number of vertical facades that serve as high-frequency noise that is not available in satellite maps. This structural gap is further complicated by micro-level scale ambiguity, where texture sizes vary drastically with depth, making feature alignment unreliable. Merely concatenating depth maps is insufficient, as raw monocular depth lacks the semantic capacity to distinguish valid matching surfaces from invalid ones.

We propose (MGS)²-Net, a novel network that shifts the CVGL solution from passive texture matching to active geometric filtering. The insight here is that robust alignment hinges on explicitly filtering out view-dependent vertical structures. To this end, we introduce a Macro-Geometric Structure Filtering (MGS-F) module to serve as the backbone of our framework. MGS-F computes dilated geometric gradients to capture large-scale planar trends, effectively suppressing vertical facade features while preserving horizontal plane structure features.

Complementing MGS-F, we introduce the Micro-Geometric Scale Adaptation (MGS-A) module to resolve the scale ambiguity that often undermines structural analysis. By applying depth priors and regressing dynamic attention weights, MGS-A fuses features from three different scale-expanding branches. Finally, the Structure-Guided Contrastive (SGC) Loss discriminates against cross-view blind spots by enforcing a margin between horizontal and vertical features.

Our contributions can be summarized as follows:

- We propose a geometry-grounded CVGL paradigm via (MGS)²-Net. To the best of our knowledge, this is the first framework to explicitly leverage 3D structural constraints to bridge the oblique-orthogonal view difference. By introducing the MGS-F module that filters out view-dependent vertical interferences, we successfully shift the considered problem from passive 2D texture matching to active 3D geometric alignment.
- We propose a synergistic combination of the MGS-A module and the SGC Loss to further improve geometric consistency. The MGS-A module utilizes depth priors to dynamically rectify scale ambiguity across varying flight altitudes, while the SGC Loss treats vertical facades as hard negatives, constraining the network to differentiate cross-view blind spots.
- We achieve new state-of-the-art performance across multiple benchmarks. Extensive experiments demonstrate that our method delivers record-breaking Recall@1 scores of 97.60% on the University-1652 dataset and 98.45% on the SUES-200 dataset. Furthermore, (MGS)²-Net exhibits strong cross-dataset generalization capabilities, verifying the superior robustness of the proposed approach against domain shifts.

2 Related Work

2.1 Foundation Models and Cross-View Geo-Localization

Cross-view geo-localization (CVGL) is normally formulated as a metric learning problem, aiming to embed location-dependent visual cues into a shared latent space [14]. Early works predominantly relied on Convolutional Neural Networks (CNNs). Approaches like CVM-Net [15] utilized NetVLAD [16] for global descriptor aggregation, while RK-Net [17] incorporated keypoint detection to focus on discriminative regions.

Recently, the introduction of Vision Transformers (ViT) and large-scale Foundation Models has marked a paradigm shift [18]. For instance, Sample4Geo [19] achieved significant gains via hard-negative mining. Concurrently, foundation models like DINO [20] and DINOv2 [21] have demonstrated exceptional generalization capabilities. Recent works [22], [23] have successfully adapted these pre-trained frozen backbones to UAV problem, utilizing their robust semantic descriptors to mitigate domain shifts. Despite their representational power, these RGB foundation models operate on a 2D manifold. Consequently, they neglect depth-induced scale ambiguities and overfit to visual interferences rather than geometrically consistent structures.

2.2 Fine-Grained Alignment and Semantic Fusion

To address the spatial misalignment inherent in global descriptors, research has shifted towards fine-grained semantic alignment [24]. Several approaches integrate high-level semantics through graph convolutional networks [25], correlation estimators [26], or coarse-to-fine regional alignments [27] to model layout consistencies. To handle diverse scene characteristics, multi-environment adaptive

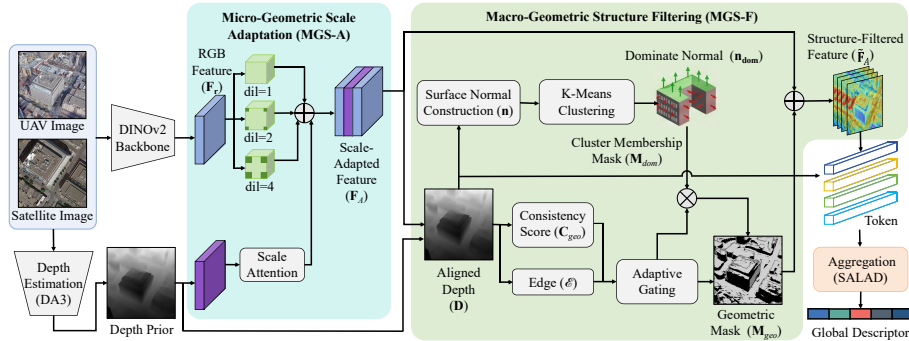


Fig. 2: Overview of the proposed geometry-grounded (MGS)²-Net framework. The pipeline decomposes cross-view alignment into two stages: micro-level scale adaptation and macro-level structural filtering, ultimately yielding view-invariant representations.

frameworks like MESAN [28] have been proposed. Other advancements focus on refining feature correspondence through hierarchical distillation [29], mixing features for robust visual place recognition [30], or unifying retrieval and reranking pipelines [31]. However, since the current semantic methods lack explicit 3D constraints, texturally similar but geometrically distinct planes are often misaligned, severely degrading the performance of CVGL.

2.3 Geometry-Aware Cross-View Geo-Localization

Recognizing the limitations of 2D texture matching, a growing number of studies have begun to incorporate geometric cues. Generative methods synthesize novel views to bridge the perspective gap, such as translating satellite imagery into street-level panoramas [32], while Wang et al. [33] utilize Neural ODEs for continuous manifold modeling. In broader place recognition tasks, LiDAR-camera fusion [34], [35] has been used to impose metric constraints. However, in standard CVGL, where only monocular images are available, existing methods almost entirely neglect the utilization of depth information [36], [37]. This 2D matching paradigm is inherently suboptimal, as it lacks the 3D geometric awareness required to differentiate between view-invariant structures and view-dependent interferences. Diverging from these conventional 2D approaches, we propose a geometry-grounded paradigm via (MGS)²-Net, where the state-of-the-art Depth Anything 3 [38] is leveraged to extract explicit depth priors.

3 Methodology

3.1 Overview

Given a query UAV image I_u and a gallery of satellite images $\mathcal{S} = \{I_s^i\}_{i=1}^N$, cross-view geo-localization aims to learn a mapping $\mathcal{F}(\cdot)$ that projects both domains into a shared latent space. A fundamental challenge is the domain gap: UAV images capture oblique views that contain vertical facades, whereas satellite images feature orthographic horizontal planes. To mitigate these view-dependent

interferences, we propose a geometry-aware framework comprising these novel components (Figure 2).

3.2 Micro-Geometric Scale Adaptation (MGS-A)

To mitigate the scale ambiguity caused by varying UAV flight altitudes, MGS-A dynamically calibrates the receptive field guided by depth cues. Given an initial RGB feature map $\mathbf{F}_r \in \mathbb{R}^{C \times H \times W}$ from the backbone [21], MGS-A generates 3 branches \mathbf{F}_k for near ($k = 1$), middle ($k = 2$), and far ($k = 3$) spatial scales:

$$\mathbf{F}_1 = \mathbf{F}_r, \quad \mathbf{F}_2 = \phi_2(\mathbf{F}_r), \quad \mathbf{F}_3 = \phi_3(\mathbf{F}_r), \quad (1)$$

where ϕ_2 and ϕ_3 denote depth-wise 3×3 convolutional layers with dilation rates of 2 and 4, respectively.

To determine the optimal scale contribution, the normalized depth map is first encoded into depth embeddings $\mathbf{F}_d \in \mathbb{R}^{C \times H \times W}$. A predictive convolutional head ψ projects \mathbf{F}_d into scale-specific logits $\mathbf{Z} = \psi(\mathbf{F}_d) \in \mathbb{R}^{3 \times H \times W}$. Let $\mathbf{Z}_k \in \mathbb{R}^{H \times W}$, $k = 1, 2, 3$, denote the k -th channel slice of \mathbf{Z} . The dynamic weight map for the k -th scale branch, $\mathbf{W}_k \in [0, 1]^{H \times W}$, is then computed via a channel-wise exponential normalization:

$$\mathbf{W}_k = \frac{\exp(\mathbf{Z}_k)}{\sum_{c=1}^3 \exp(\mathbf{Z}_c)}. \quad (2)$$

The scale-adaptive feature $\mathbf{F}_A \in \mathbb{R}^{C \times H \times W}$ is obtained via a weighted fusion, followed by a residual connection to preserve the original semantic information:

$$\mathbf{F}_A = \mathbf{F}_r + \sum_{k=1}^3 \mathbf{W}_k \odot \mathbf{F}_k, \quad (3)$$

where \mathbf{W}_k represents the k -th spatial slice of the weight tensor broadcasted along the channel dimension, and \odot denotes the Hadamard product. The resulting feature map \mathbf{F}_A possesses enhanced scale invariance and serves as the refined input to the subsequent structure filtering module.

3.3 Macro-Geometric Structure Filtering (MGS-F)

MGS-F extracts a dominant geometric normal as a robust prior to indicate the co-visible planar direction, effectively suppressing cross-view blind spots.

Macro Gradient and Edge Perception. Given a bilinearly aligned raw depth map $\mathbf{D} \in \mathbb{R}^{H \times W}$, we compute depth gradients using dilated Sobel convolutions to capture large-scale planar orientations while suppressing local roughness:

$$\mathbf{G}_x = \mathbf{D} * \mathbf{S}_x^{(r)}, \quad \mathbf{G}_y = \mathbf{D} * \mathbf{S}_y^{(r)}, \quad (4)$$

where $*$ denotes the convolution operation, and $\mathbf{S}_x^{(r)}, \mathbf{S}_y^{(r)}$ are predefined horizontal and vertical Sobel kernels with a dilation rate of r .

To identify and suppress discontinuity-dominated regions, we compute the gradient magnitude tensor $\mathbf{G}_{mag} = \sqrt{\mathbf{G}_x^2 + \mathbf{G}_y^2}$, where the operations are applied element-wise. High-frequency ambiguous edges are flagged using a binary mask $\mathbf{M}_{edge} = \mathbb{I}(\mathbf{G}_{mag} > \tau_{grad})$, where the logical inequality is evaluated element-wise across the spatial dimensions, $\mathbb{I}(\cdot)$ denotes the indicator function, and $\tau_{grad} \in \mathbb{R}$ is an adaptive scalar threshold.

Dominant Plane Perception via Normal Clustering. The dense surface normal tensor $\mathbf{N} \in \mathbb{R}^{3 \times H \times W}$ is analytically constructed from the derived gradients via L_2 normalization along the channel dimension:

$$\mathbf{N} = \frac{[-\mathbf{G}_x, -\mathbf{G}_y, \mathbf{1}]}{\|[-\mathbf{G}_x, -\mathbf{G}_y, \mathbf{1}]\|_2}, \quad (5)$$

where $[\cdot, \cdot]$ denotes channel-wise concatenation and $\mathbf{1} \in \mathbb{R}^{H \times W}$ is an all-ones tensor matching the spatial dimensions.

To robustly identify the co-visible plane, we perform K-Means clustering using cosine similarity on the normal vectors strictly outside the edge regions. This partitions the spatial normals, from which we extract the centroid of the largest cluster as the dominant normal vector $\mathbf{n}_{dom} \in \mathbb{R}^3$. Concurrently, the spatial footprint of this cluster is captured by a binary indicator mask $\mathbf{M}_{dom} \in \{0, 1\}^{H \times W}$, where values are 1 if the corresponding normal belongs to the dominant cluster.

Subsequently, the continuous geometric consistency map $\mathbf{C}_{geo} \in \mathbb{R}^{H \times W}$ is computed by projecting the local normals onto this dominant direction:

$$\mathbf{C}_{geo} = \mathbf{n}_{dom}^\top \mathbf{N}, \quad (6)$$

where the projection is applied along the channel dimension of \mathbf{N} .

Adaptive Gating and Residual Modulation. A learnable Sigmoid activation $\sigma(\cdot)$ with scale s and bias β is applied to the consistency map. To prevent destructive modulation on ambiguous boundaries, regions identified by the edge mask are strictly rectified to a learnable neutral prior μ . The unified continuous geometric mask tensor $\mathbf{M}_{geo} \in [0, 1]^{H \times W}$ is formulated as:

$$\mathbf{M}_{geo} = (\mathbf{1} - \mathbf{M}_{edge}) \odot \left(\sigma(s\mathbf{C}_{geo} + \beta) \odot \mathbf{M}_{dom} \right) + \mu\mathbf{M}_{edge}, \quad (7)$$

where $\mu \in \mathbb{R}$ is a learnable scalar initialized to 0.5 to represent the baseline structural confidence. This robust geometric prior is then injected into the semantic stream via additive residual modulation:

$$\tilde{\mathbf{F}}_A = \mathbf{F}_A + \lambda\mathbf{M}_{geo}, \quad (8)$$

where λ is a learnable scalar balancing the geometric injection, and the spatial mask \mathbf{M}_{geo} is broadcast along the channel dimension to match the shape of \mathbf{F}_A . This design strictly preserves the underlying semantic stability while actively highlighting the structural cues of co-visible planes.

Depth-Conditioned Global Aggregation. Given the depth embeddings $\mathbf{F}_d \in \mathbb{R}^{C \times H \times W}$ previously encoded in MGS-A, a spatial attention gate is generated via a lightweight 1×1 convolutional bottleneck ϕ_{spa} to selectively enrich the semantic features $\tilde{\mathbf{F}}_A \in \mathbb{R}^{C \times H \times W}$:

$$\hat{\mathbf{F}}_A = \tilde{\mathbf{F}}_A \odot (\mathbf{1} + \phi_{spa}(\mathbf{F}_d)), \quad (9)$$

where $\phi_{spa}(\mathbf{F}_{dep}) \in \mathbb{R}^{H \times W}$ acts as a spatial modulator and is broadcast along the channel dimension. To explicitly embed 3D spatial awareness, the 2D grid coordinates $\mathbf{P}_{grid} \in \mathbb{R}^{2 \times H \times W}$ are channel-wise concatenated with the aligned depth map $\mathbf{D} \in \mathbb{R}^{H \times W}$. A spatial bias is then injected using a neural mapping function φ_{pos} , which projects the $3 \times H \times W$ joint coordinate tensor into the semantic space:

$$\mathbf{F}_{agg} = \hat{\mathbf{F}}_A + \gamma \varphi_{pos}([\mathbf{D}; \mathbf{P}_{grid}]), \quad (10)$$

where $\gamma \in \mathbb{R}$ is a learnable scalar, and $\mathbf{F}_{agg} \in \mathbb{R}^{C \times H \times W}$ represents the spatially enriched feature map. Finally, \mathbf{F}_{agg} and the semantic tokens are processed through the core SALAD aggregation module [39], leveraging Sinkhorn optimal transport and a dustbin mechanism, followed by L_2 normalization to yield the final global descriptor.

3.4 Structure-Guided Contrastive (SGC) Loss

To prevent the backbone from implicitly overfitting to prominent vertical textures, we propose SGC, ensuring stronger feature activation on co-visible planes than on hard negatives.

Geometric Partitioning. We define two binary partitioning masks for the co-visible regions ($\mathbf{M}_{\mathcal{P}}$) and non-co-visible regions ($\mathbf{M}_{\mathcal{N}}$):

$$\mathbf{M}_{\mathcal{P}} = \mathbb{I}(\mathbf{M}_{geo} > \tau_{high}), \quad \mathbf{M}_{\mathcal{N}} = \mathbb{I}(\mathbf{M}_{geo} < \tau_{low}), \quad (11)$$

where $\mathbb{I}(\cdot)$ denotes the indicator function, and both logical inequalities are evaluated element-wise across the spatial dimensions. The variables $\tau_{high}, \tau_{low} \in \mathbb{R}$ represent dynamically computed scalar thresholds for each image.

Activation Aggregation. To quantify the network’s spatial attention, we define the semantic activation map $\mathbf{A}_{sem} \in \mathbb{R}^{H \times W}$ as the channel-wise mean absolute magnitude of the geometrically enhanced features $\tilde{\mathbf{F}}_A$:

$$\mathbf{A}_{sem} = \frac{1}{C} \sum_{c=1}^C |\tilde{\mathbf{F}}_{A,c}|, \quad (12)$$

where c denotes the channel index. We then aggregate the mean activation intensities for the partitioned regions. The average activations $v_{\mathcal{P}}$ and $v_{\mathcal{N}}$ for the partitioned regions are formulated as:

$$v_{\mathcal{P}} = \frac{\|\mathbf{A}_{sem} \odot \mathbf{M}_{\mathcal{P}}\|_1}{\|\mathbf{M}_{\mathcal{P}}\|_1}, \quad v_{\mathcal{N}} = \frac{\|\mathbf{A}_{sem} \odot \mathbf{M}_{\mathcal{N}}\|_1}{\|\mathbf{M}_{\mathcal{N}}\|_1}. \quad (13)$$

The scalars $v_{\mathcal{P}}$ and $v_{\mathcal{N}}$ represent the network’s mean response to invariant co-visible planes and variant vertical facades, respectively.

Contrastive Ranking Objective. The SGC loss enforces a predefined margin ξ to penalize higher activations on facade-like regions compared to horizontal planes. We formulate this objective using the standard hinge loss notation:

$$\mathcal{L}_{SGC} = [v_{\mathcal{N}} - v_{\mathcal{P}} + \xi]_+, \quad (14)$$

where $[\cdot]_+ = \max(0, \cdot)$ denotes the standard hinge operation. As a semantic rectifier, \mathcal{L}_{SGC} distills relative activation ordering into the feature representations.

3.5 Optimization Objective

The overall training objective combines the primary place-retrieval loss with the proposed geometric constraint:

$$\mathcal{L}_{total} = \mathcal{L}_{ret} + \lambda_{geo} \mathcal{L}_{SGC}, \quad (15)$$

where \mathcal{L}_{ret} is the baseline metric learning objective, i.e., the Multi-Similarity loss [40], and λ_{geo} is a scaling factor balancing the geometric regularization.

4 Experiments

4.1 Datasets and Evaluation Metrics

To evaluate the effectiveness of the proposed framework, we conducted experiments on two standard benchmarks: University-1652 [41] and SUES-200 [42].

University-1652 is a large-scale multi-view dataset containing 1,652 buildings from 72 universities. It includes 50,218 drone-view images for training and 37,855

for testing, paired with corresponding satellite orthophotos. This dataset is particularly challenging due to the inclusion of drone images captured at varying distances and angles.

SUES-200 focuses on multi-altitude scenarios, covering 200 disparate locations. It provides drone images captured at four distinct altitudes (150m, 200m, 250m, and 300m). This multi-level height design allows for a fine-grained assessment of the model’s robustness against scale variations.

Following standard protocols, we employ Recall at K (R@K) and Average Precision (AP) as the primary metrics. R@K measures the percentage of query images for which the ground truth is retrieved within the top-K predictions, while AP evaluates the precision of the retrieval ranking.

4.2 Implementation Details

We implement (MGS)²-Net using the PyTorch framework on a single NVIDIA A800 GPU. During the training phase, the input images for both satellite and drone views are resized to 224×224 . For inference, we adopt a higher resolution of 336×336 to capture fine-grained geometric details. We utilize a pre-trained DINOv2-B [21] as the backbone to extract initial semantic features and AdamW with a weight decay of 9.5×10^{-9} . A linear learning rate schedule is applied. The batch size is 128. We employ parameter-wise learning rates: 2×10^{-5} for the RGB backbone, 5×10^{-5} for depth-related backbone (depth encoder + MGS-F + MGS-A), and 1×10^{-4} for the aggregator. The hyper-parameters for SGC loss, i.e., λ_{geo} and ξ , are empirically set to 1.0 and 0.5, respectively. During inference, we utilize the cosine similarity of the final fused embeddings for retrieval ranking.

To prevent overfitting and reduce computational overhead, we freeze the majority of the pre-trained backbone during the training phase. Consequently, our (MGS)²-Net framework comprises a total of 115.56M parameters, of which only 32.91M are trainable. This parameter-efficient design allows the network to focus on optimizing the proposed MGS-A and MGS-F modules, ensuring fast convergence and low training costs.

4.3 Comparison with State-of-the-Art Methods

Performance on University-1652. We compare (MGS)²-Net against recent state-of-the-art (SOTA) methods, including geometric-aware approaches like GeoFormer and semantic-enhanced methods like CAMP [49] and QDFL [51]. The quantitative results are summarized in Table 1.

It can be seen that (MGS)²-Net achieves superior performance across all metrics. In particular, in the Drone→Satellite task, our method achieves a Recall@1 of 97.60% and an AP of 98.03%. This represents a significant improvement over the runner-up JRN-Geo [53] (+2.47% in R@1) and QDFL [51] (+2.60% in R@1). Unlike methods that treat the image as a 2D plane, our framework explicitly models the 3D structure. The substantial gain indicates that our method ensures that hard-negative facade features do not confuse the retrieval ranking.

Table 1: Performance Comparison on the University-1652 Dataset. The Best Results Are in Bold.

Method	Test Image Size	Drone \rightarrow Satellite		Satellite \rightarrow Drone	
		R@1	AP	R@1	AP
Safe-Net [43]	256 \times 256	86.98	88.85	91.22	86.06
GeoFormer [23]	224 \times 224	89.08	90.83	92.30	88.54
MCCG [44]	384 \times 384	89.64	91.32	94.30	89.39
SDPL [45]	256 \times 256	90.16	91.64	93.58	89.45
CCR [46]	384 \times 384	92.54	93.78	95.15	91.80
Sample4Geo [19]	384 \times 384	92.65	93.81	96.43	93.79
SRLN [24]	384 \times 384	92.70	93.77	95.14	91.97
MEAN [47]	384 \times 384	93.55	94.53	96.01	92.08
SCOF [48]	384 \times 384	93.68	94.68	96.29	92.68
CAMP [49]	384 \times 384	94.46	95.38	96.15	92.72
DAC [50]	384 \times 384	94.67	95.50	96.43	93.79
QDFL [51]	280 \times 280	95.00	95.83	97.15	94.57
CDM-Net [52]	512 \times 512	95.13	96.04	96.43	93.79
JRN-Geo [53]	384 \times 384	95.13	95.85	96.72	94.93
Ours	336 \times 336	97.60	98.03	98.86	97.25

Robustness to Scale Variations on SUES-200. We also evaluate our method on SUES-200 across different flight altitudes. As shown in Table 2, (MGS)²-Net exhibits remarkable robustness. While most existing methods, such as CDM-Net [52], suffer from performance degradation at lower altitudes (150m) due to the impact of more vertical facades, (MGS)²-Net maintains a high R@1 of 98.45% at 150m on the Drone \rightarrow Satellite task. As the altitude increases to 300m, the performance of the proposed method reaches the maximum value, achieving a perfect 100% R@1. The reason for maintaining extremely high recall at high altitudes is that our MGS-A module provides a more physically grounded solution to scale ambiguity. Compared to MEAN [47], which employs multi-level embeddings, our approach still outperforms it at 300m altitude. Notably, on the Satellite \rightarrow Drone task, apart from the challenging 150m altitude, the results on other altitudes have achieved 100% R@1. This indicates that the localization task in this scenario has been completely resolved.

Cross-Dataset Generalization. A critical bottleneck for learning-based CVGL is overfitting to the source domain’s specific architectural style. To comprehensively test generalization capabilities, we train our model solely on the University-1652 dataset and directly evaluate it under two distinct zero-shot transfer scenarios: varying altitudes (SUES-200) and severe stylistic shifts (DenseUAV).

First, we evaluate the generalization performance on the SUES-200 dataset to verify robustness against unseen scale variations. As illustrated in Fig. 3, despite the absence of target-domain training data, (MGS)²-Net consistently achieves the best retrieval performance across all altitude sub-datasets when

Table 2: Performance Comparison Between Different Methods on Drone-to-Satellite and Satellite-to-Drone Retrieval Tasks. The Best Results Are in Bold.

Drone→Satellite									
Method	Test Image Size	150m		200m		250m		300m	
		R@1	AP	R@1	AP	R@1	AP	R@1	AP
SUES-200 [42]	384 × 384	59.32	64.93	62.30	67.24	71.35	75.49	77.17	67.80
Safe-Net [43]	256 × 256	81.05	84.76	91.10	93.04	94.52	95.74	94.57	95.60
MCCG [44]	384 × 384	82.22	85.47	89.38	91.41	93.82	95.04	95.07	96.20
SDPL [45]	256 × 256	82.95	85.82	92.73	94.07	96.05	96.69	97.83	98.05
CCR [46]	384 × 384	87.08	89.55	93.57	94.90	95.42	96.28	96.82	97.39
Sample4Geo [19]	384 × 384	92.60	96.38	97.38	97.81	98.28	98.64	99.18	99.36
SRLN [24]	384 × 384	89.90	91.90	94.32	95.65	95.92	96.79	96.37	97.21
SCOF [48]	384 × 384	90.75	92.32	94.25	95.35	96.88	97.42	97.85	98.10
QDFL [51]	280 × 280	93.97	95.42	98.25	98.67	99.30	99.48	99.31	99.48
CDM-Net [52]	512 × 512	93.78	95.16	97.62	98.16	98.28	98.69	99.20	99.31
CAMP [49]	384 × 384	95.40	96.38	97.63	98.16	98.05	98.45	99.33	99.46
MEAN [47]	384 × 384	95.50	96.46	98.38	98.72	98.95	99.17	99.52	99.63
DAC [50]	384 × 384	96.80	97.54	97.48	97.97	98.20	98.62	97.58	98.14
Ours	336 × 336	98.45	98.78	99.62	99.69	99.78	99.80	100.00	100.00
Satellite→Drone									
Method	Test Image Size	150m		200m		250m		300m	
		R@1	AP	R@1	AP	R@1	AP	R@1	AP
SUES-200	384 × 384	82.50	58.95	85.00	62.56	88.75	69.96	96.25	84.16
MCCG	384 × 384	93.75	89.72	93.75	92.21	96.25	96.14	98.75	96.64
SDPL	384 × 384	93.75	83.75	96.25	92.42	97.50	95.65	96.25	96.17
CCR	384 × 384	92.50	88.54	97.50	95.22	97.50	97.10	97.50	97.49
Sample4Geo	384 × 384	97.50	93.63	98.75	96.70	98.75	98.28	98.75	98.05
SRLN	384 × 384	93.75	93.01	97.50	95.08	97.50	96.52	97.50	96.71
SCOF	384 × 384	95.00	89.72	97.50	93.13	98.75	96.33	97.50	96.62
CDM-Net	384 × 384	95.25	92.24	98.50	96.40	99.00	97.60	99.00	98.01
CAMP	384 × 384	96.25	93.69	97.50	96.76	98.75	98.10	100.00	98.85
Safe-Net	256 × 256	97.50	86.36	96.25	92.61	97.50	94.98	98.75	95.67
DAC	384 × 384	97.50	94.06	98.75	96.66	98.75	98.09	98.75	97.87
MEAN	384 × 384	97.50	94.75	100.00	97.09	100.00	98.28	100.00	99.21
QDFL	384 × 384	98.75	95.10	98.75	97.92	100.00	99.07	100.00	99.07
Ours	336 × 336	98.75	96.50	100.00	98.51	100.00	98.73	100.00	98.95

compared with state-of-the-art methods. This demonstrates that our scale adaptation mechanism effectively generalizes to novel environments.

To further test the model’s robustness, we evaluate it on the DenseUAV dataset [54], as detailed in Table 3. In this extreme zero-shot transfer case, most existing methods collapse on the retrieval task. As noted by SURFNet [55], DenseUAV presents a significant challenge because it possesses stronger photometric and stylistic domain gaps, alongside much denser urban coverage. Consequently, methods relying on texture or passive attention fail to generalize. For instance, CAMP [49] yields only 23.48% R@1. In contrast, our method maintains a remarkable Recall@1 of 84.60%.

This dramatic performance gap suggests that (MGS)²-Net learns intrinsic geometric properties rather than dataset-specific texture patterns. By physically filtering out non-transferable vertical facades, the model robustly focuses on the

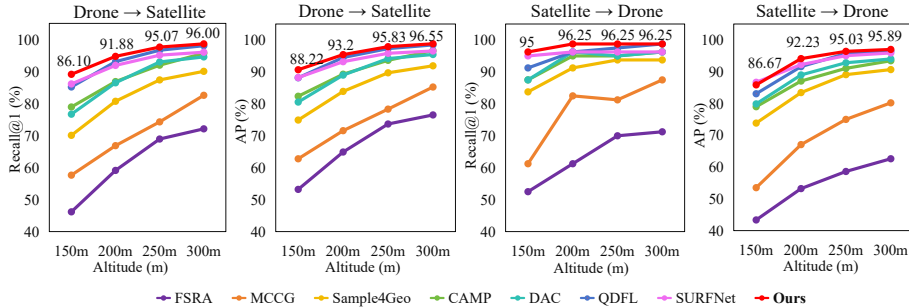


Fig. 3: Visualizations of generalization results on SUES-200 dataset compared with state-of-the-art methods, using University-1652 only as the training set.

Table 3: Generalization from University-1652 to DenseUAV.

Method	UAV→Satellite		Satellite→UAV	
	R@1	AP	R@1	AP
Sample4Geo [19]	22.00	14.58	19.10	17.46
CAMP [49]	23.48	15.75	20.97	20.29
SURFNet (Zero shot) [55]	24.28	16.13	21.04	20.37
SURFNet (Fine-tune) [55]	71.06	65.99	87.43	51.29
Ours (Zero shot)	84.60	67.33	77.05	68.89

Table 4: Component-wise Ablation Analysis on the University-1652 Drone-to-Satellite Retrieval Task.

Model	MGS-A	MGS-F	SGC	R@1	AP
Baseline I (w/o Depth)				92.05	93.34
Baseline II (w/ Depth)				94.24	95.02
Ours I	✓			95.13 _{+0.89}	95.90 _{+0.88}
Ours II	✓	✓		97.32 _{+3.08}	97.67 _{+2.65}
Ours III (Full)	✓	✓	✓	97.60_{+3.36}	98.03_{+3.01}

structural "fingerprint" of co-visible planes, which inherently remains invariant across diverse cities and altitudes.

4.4 Ablation Studies

To verify the individual contributions of each component in (MGS)²-Net, we conducted a comprehensive step-wise ablation study on the University-1652 drone-to-satellite retrieval task. The quantitative results are summarized in Table 4.

Starting from the Baseline I (DINOv2-B [21] + SALAD [39], without depth prior), which yields 92.05% Recall@1, we first validate the necessity of the depth modality and its integration strategy. To further show the architectural contribution, Baseline II implements a naive fusion baseline by explicitly concatenating

the depth features with Baseline I. While this simple concatenation provides a noticeable baseline improvement (to 94.24% R@1), it remains sub-optimal for handling the severe scale ambiguity caused by varying drone flight altitudes. The improvement indicated by the subscript numbers in the lower half of Table 4 is measured relative to Baseline II.

By replacing the naive concatenation with our MGS-A module (Ours I), the network explicitly utilizes depth priors to dynamically re-weight multi-scale features. While this yields a modest direct numerical gain (to 95.13% R@1), its primary architectural contribution lies in functionally aligning the multi-scale features with physical depth, serving as a critical geometric foundation for subsequent processing.

Building upon this, the addition of the MGS-F module (Ours II) further elevates the R@1 to 97.32% (a +2.19% increase). A qualitative analysis and visualization of the MGS-F module, along with further discussion of its mechanism of action, will be presented in the next subsection.

Finally, combining both modules with the SGC Loss (Ours III) yields the full (MGS)²-Net framework, achieving the best performance. The SGC Loss acts as a crucial rectifier during the training phase, ensuring that the feature representations inherently maintain the correct geometric activation ordering even when facing complex architectural layouts.

4.5 Qualitative Analysis and Visualization

To provide intuitive insights into how (MGS)²-Net bridges the domain gap, we present visualizations of feature responses and retrieval results.

Visualization of Geometric Filtering. Fig. 4 visualizes the feature activation maps before and after applying MGS-F. Fig. 4(b) clearly demonstrates that MGS-F successfully predicts horizontal planes (white area) and vertical planes (black area). Using this as a mask, it forces the feature map to focus more on horizontal plane features rather than vertical ones. This is also well indicated on the feature map: horizontal planes within the white box are effectively enhanced, while vertical planes within the black box are suppressed. This verifies that MGS-F functions not merely as an attention mechanism, but as a physical filter that aligns the drone view with the orthographic satellite map.

Retrieval Results. We further compared the top 5 retrieval results between the baseline and (MGS)²-Net and selected representative examples as shown in Figure 5. As demonstrated in the second and fourth rows, the baseline retrieves candidates with similar facade textures but different structural layouts, leading to false positives. For instance, in the UAV→Satellite task, the baseline (row 2) tends to recall results containing red features during retrieval because the query facade texture exhibits red features. In contrast, (MGS)²-Net (row 1) correctly retrieves the target location while ignoring the red features. In the Satellite→UAV task, a challenging case involves a roof with large white features. (MGS)²-Net actively focuses on the roof structure while suppressing excessive

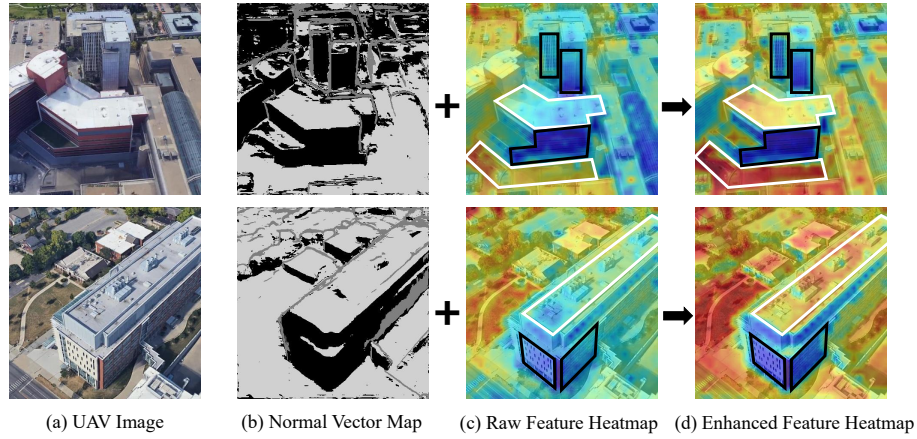


Fig. 4: Visualization of the MGS-F mechanism. We visualize the feature response maps before and after applying MGS-F. (b) The white area indicates that the normal vector points vertically upward, while the black area indicates that the normal vector is nearly parallel to the ground. (c) The backbone naively activates texture-rich regions. (d) MGS-F redistributes attention based on geometric priors. Note that black boxes indicate the effective suppression of view-dependent vertical facades, while white boxes highlight the adaptive enhancement of view-invariant horizontal planes.

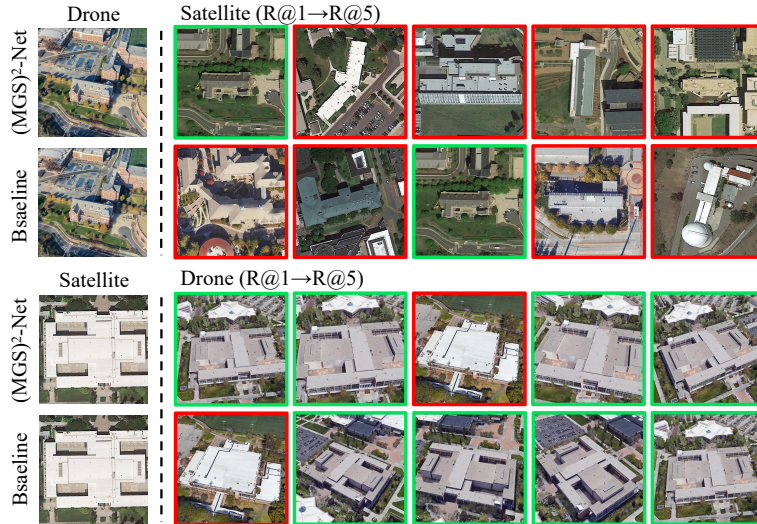


Fig. 5: Qualitative retrieval results for the University-1652 dataset. (Top) Top 5 retrieval results for the drone to satellite retrieval task. (Bottom) Top 5 retrieval results for the satellite to drone retrieval task. The first and third rows show retrieval results for (MGS)²-Net, while the second and fourth rows show retrieval results for the baseline. **Green** borders indicate correct matches and **red** borders indicate incorrect matches.

RGB influence, finding the correct candidate. This is particularly common in

densely built environments, where our method’s ability to suppress non-co-visible regions in cross-view pairs is crucial for accurate localization.

5 CONCLUSION

In this paper, we presented (MGS)²-Net, a geometry-grounded framework that bridges the UAV-satellite domain gap by shifting from 2D appearance matching to 3D structural alignment. By synergizing the Macro-Geometric Structure Filtering (MGS-F) to suppress vertical interferences and the Micro-Geometric Scale Adaptation (MGS-A) to rectify scale discrepancies, our method effectively extracts view-invariant geometric features. Extensive experiments demonstrate that (MGS)²-Net achieves state-of-the-art performance on University-1652 and SUES-200 benchmarks. Future work will focus on distilling the geometric awareness into a lightweight backbone for real-time edge deployment and improving robustness against extreme illumination variations.

References

1. Yuekuan Zhou. Unmanned aerial vehicles based low-altitude economy with lifecycle techno-economic-environmental analysis for sustainable and smart cities. *Journal of Cleaner Production*, 499:145050, 2025. [1](#)
2. Tazeem Ahmad, Alicia Esquivel Morel, Nuo Cheng, Kannappan Palaniappan, Prasad Calyam, Kun Sun, and Jianli Pan. Future uav/drone systems for intelligent active surveillance and monitoring. *ACM Computing Surveys*, 58(2):35:1–35:37, 2026. [1](#)
3. Gabriele Berton, Carlo Masone, and Barbara Caputo. Rethinking visual geo-localization for large-scale applications. In *Proceedings of the IEEE/CVF Conference on Computer Vision and Pattern Recognition*, pages 4878–4888, 2022. [1](#)
4. Yujiao Shi, Xin Yu, Liu Liu, Dylan Campbell, Piotr Koniusz, and Hongdong Li. Accurate 3-dof camera geo-localization via ground-to-satellite image matching. *IEEE Transactions on Pattern Analysis and Machine Intelligence*, 45(3):2682–2697, 2022. [1](#)
5. Xiwu Zhang, Lei Wang, and Yan Su. Visual place recognition: A survey from deep learning perspective. *Pattern Recognition*, 113:107760, 2021. [1](#)
6. Guopeng Li, Ming Qian, and Gui-Song Xia. Unleashing unlabeled data: A paradigm for cross-view geo-localization. In *Proceedings of the IEEE/CVF Conference on Computer Vision and Pattern Recognition (CVPR)*, pages 16719–16729, June 2024. [1](#)
7. Zhedong Zheng, Yunchao Wei, and Yi Yang. University-1652: A multi-view multi-source benchmark for drone-based geo-localization. In *Proceedings of the 28th ACM international conference on Multimedia*, pages 1395–1403, 2020. [1](#)
8. Tingyu Wang, Zhedong Zheng, Chenggang Yan, Jiyong Zhang, Yaoqi Sun, Bolun Zheng, and Yi Yang. Each part matters: Local patterns facilitate cross-view geo-localization. *IEEE Transactions on Circuits and Systems for Video Technology*, 32(2):867–879, 2021. [1](#)
9. Yujiao Shi, Liu Liu, Xin Yu, and Hongdong Li. Spatial-aware feature aggregation for image based cross-view geo-localization. *Advances in Neural Information Processing Systems*, 32, 2019. [1](#)

10. Sijie Zhu, Mubarak Shah, and Chen Chen. Transgeo: Transformer is all you need for cross-view image geo-localization. In *Proceedings of the IEEE/CVF Conference on Computer Vision and Pattern Recognition*, pages 1162–1171, 2022. [1](#)
11. Hongji Yang, Xiufan Lu, and Yingying Zhu. Cross-view geo-localization with layer-to-layer transformer. *Advances in Neural Information Processing Systems*, 34:29009–29020, 2021. [1](#)
12. Zeng Lu, Tao Pu, Tianshui Chen, and Liang Lin. Content-aware hierarchical representation selection for cross-view geo-localization. In *Proceedings of the Asian Conference on Computer Vision*, pages 4211–4224, 2022. [2](#)
13. Feng Lu, Xiangyuan Lan, Lijun Zhang, Dongmei Jiang, Yaowei Wang, and Chun Yuan. Cricavpr: Cross-image correlation-aware representation learning for visual place recognition. In *Proceedings of the IEEE/CVF Conference on Computer Vision and Pattern Recognition*, pages 16772–16782, 2024. [2](#)
14. Krishna Regmi and Mubarak Shah. Bridging the domain gap for ground-to-aerial image matching. In *Proceedings of the IEEE/CVF International Conference on Computer Vision*, pages 470–479, 2019. [3](#)
15. Sixing Hu, Mengdan Feng, Rang MH Nguyen, and Gim Hee Lee. Cvm-net: Cross-view matching network for image-based ground-to-aerial geo-localization. In *Proceedings of the IEEE Conference on Computer Vision and Pattern Recognition*, pages 7258–7267, 2018. [3](#)
16. Relja Arandjelovic, Petr Gronat, Akihiko Torii, Tomas Pajdla, and Josef Sivic. Netvlad: Cnn architecture for weakly supervised place recognition. In *Proceedings of the IEEE Conference on Computer Vision and Pattern Recognition*, pages 5297–5307, 2016. [3](#)
17. Jinliang Lin, Zhedong Zheng, Zhun Zhong, Zhiming Luo, Shaozi Li, Yi Yang, and Nicu Sebe. Joint representation learning and keypoint detection for cross-view geo-localization. *IEEE Transactions on Image Processing*, 31:3780–3792, 2022. [3](#)
18. Alexey Dosovitskiy, Lucas Beyer, Alexander Kolesnikov, Dirk Weissenborn, Xiuhua Zhai, Thomas Unterthiner, Mostafa Dehghani, Matthias Minderer, Georg Heigold, Sylvain Gelly, et al. An image is worth 16x16 words: Transformers for image recognition at scale. *arXiv preprint arXiv:2010.11929*, 2020. [3](#)
19. Fabian Deuser, Konrad Habel, and Norbert Oswald. Sample4geo: Hard negative sampling for cross-view geo-localisation. In *Proceedings of the IEEE/CVF International Conference on Computer Vision*, pages 16847–16856, 2023. [3](#), [10](#), [11](#), [12](#)
20. Mathilde Caron, Hugo Touvron, Ishan Misra, Hervé Jégou, Julien Mairal, Piotr Bojanowski, and Armand Joulin. Emerging properties in self-supervised vision transformers. In *Proceedings of the IEEE/CVF International Conference on Computer Vision*, pages 9650–9660, 2021. [3](#)
21. Maxime Oquab, Timothée Darcet, Théo Moutakanni, Huy Vo, Marc Szafraniec, Vasil Khalidov, Pierre Fernandez, Daniel Haziza, Francisco Massa, Alaaeldin El-Nouby, et al. DINOv2: Learning Robust Visual Features without Supervision. *Transactions on Machine Learning Research Journal*, pages 1–31, 2024. [3](#), [5](#), [9](#), [12](#)
22. Nikhil Keetha, Avneesh Mishra, Jay Karhade, Krishna Murthy Jatavallabhula, Sebastian Scherer, Madhava Krishna, and Sourav Garg. Anyloc: Towards universal visual place recognition. *IEEE Robotics and Automation Letters*, 9(2):1286–1293, 2023. [3](#)
23. Qingge Li, Xiaogang Yang, Jiwei Fan, Ruitao Lu, Bin Tang, Siyu Wang, and Shuang Su. Geoformer: An effective transformer-based siamese network for uav geolocalization. *IEEE Journal of Selected Topics in Applied Earth Observations and Remote Sensing*, 17:9470–9491, 2024. [3](#), [10](#)

24. Hongxiang Lv, Hai Zhu, Runzhe Zhu, Fei Wu, Chunyuan Wang, Meiyu Cai, and Kaiyu Zhang. Direction-guided multiscale feature fusion network for geo-localization. *IEEE Transactions on Geoscience and Remote Sensing*, 62:1–13, 2024. [3](#), [10](#), [11](#)
25. Xiangzeng Liu, Ziyao Wang, Yue Wu, and Qiguang Miao. Segcn: A semantic-aware graph convolutional network for uav geo-localization. *IEEE Journal of Selected Topics in Applied Earth Observations and Remote Sensing*, 17:6055–6066, 2024. [3](#)
26. Xiaolong Wang, Runsen Xu, Zhuofan Cui, Zeyu Wan, and Yu Zhang. Fine-grained cross-view geo-localization using a correlation-aware homography estimator. *Advances in Neural Information Processing Systems*, 36:5301–5319, 2023. [3](#)
27. Sijie Zhu, Taojiannan Yang, and Chen Chen. Vigor: Cross-view image geo-localization beyond one-to-one retrieval. In *Proceedings of the IEEE/CVF Conference on Computer Vision and Pattern Recognition*, pages 3640–3649, 2021. [3](#)
28. Tingyu Wang, Zhedong Zheng, Yaoqi Sun, Chenggang Yan, Yi Yang, and Tat-Seng Chua. Multiple-environment self-adaptive network for aerial-view geo-localization. *Pattern Recognition*, 152:110363, 2024. [4](#)
29. Jian Sun, Kangdao Liu, Chi Zhang, Chuanguan Chen, Junge Shen, CL Chen, and Chi-Man Vong. Mobilegeo: Exploring hierarchical knowledge distillation for resource-efficient cross-view drone geo-localization. *arXiv preprint arXiv:2510.22582*, 2025. [4](#)
30. Amar Ali-Bey, Brahim Chaib-Draa, and Philippe Giguere. Mixvpr: Feature mixing for visual place recognition. In *Proceedings of the IEEE/CVF Winter Conference on Applications of Computer Vision*, pages 2998–3007, 2023. [4](#)
31. Sijie Zhu, Linjie Yang, Chen Chen, Mubarak Shah, Xiaohui Shen, and Heng Wang. R2former: Unified retrieval and reranking transformer for place recognition. In *Proceedings of the IEEE/CVF Conference on Computer Vision and Pattern Recognition*, pages 19370–19380, 2023. [4](#)
32. Junyan Ye, Zhutao Lv, Weijia Li, Jinhua Yu, Haote Yang, Huaping Zhong, and Conghui He. Cross-view image geo-localization with panorama-bev co-retrieval network. In *European Conference on Computer Vision*, pages 74–90. Springer, 2024. [4](#)
33. Sijie Wang, Rui She, Qiyu Kang, Siqi Li, Disheng Li, Tianyu Geng, Shangshu Yu, and Wee Peng Tay. Multi-modal aerial-ground cross-view place recognition with neural odes. In *Proceedings of the Computer Vision and Pattern Recognition Conference*, pages 11717–11728, 2025. [4](#)
34. Zijie Zhou, Jingyi Xu, Guangming Xiong, and Junyi Ma. Lcpr: A multi-scale attention-based lidar-camera fusion network for place recognition. *IEEE Robotics and Automation Letters*, 9(2):1342–1349, 2023. [4](#)
35. Alex Junho Lee, Seungwon Song, Hyungtae Lim, Woojoo Lee, and Hyun Myung. (lc)²: Lidar-camera loop constraints for cross-modal place recognition. *IEEE Robotics and Automation Letters*, 8(6):3589–3596, 2023. [4](#)
36. Abhilash Durgam, Sidike Paheding, Vikas Dhiman, and Vijay Devabhaktuni. Cross-view geo-localization: a survey. *IEEE Access*, 12:192028–192050, 2024. [4](#)
37. Yujiao Shi, Xin Yu, Liu Liu, Tong Zhang, and Hongdong Li. Optimal feature transport for cross-view image geo-localization. In *Proceedings of the AAAI Conference on Artificial Intelligence*, volume 34, pages 11990–11997, 2020. [4](#)
38. Haotong Lin, Sili Chen, Junhao Liew, Donny Y Chen, Zhenyu Li, Guang Shi, Jiashi Feng, and Bingyi Kang. Depth anything 3: Recovering the visual space from any views. *arXiv preprint arXiv:2511.10647*, 2025. [4](#)

39. Sergio Izquierdo and Javier Civera. Optimal transport aggregation for visual place recognition. In *Proceedings of the IEEE/CVF Conference on Computer Vision and Pattern Recognition*, pages 17658–17668, 2024. 7, 12
40. Xun Wang, Xintong Han, Weilin Huang, Dengke Dong, and Matthew R Scott. Multi-similarity loss with general pair weighting for deep metric learning. In *Proceedings of the IEEE/CVF Conference on Computer Vision and Pattern Recognition*, pages 5022–5030, 2019. 8
41. Zhedong Zheng, Yunchao Wei, and Yi Yang. University-1652: A multi-view multi-source benchmark for drone-based geo-localization. In *Proceedings of the 28th ACM International Conference on Multimedia*, pages 1395–1403, 2020. 8
42. Runzhe Zhu, Ling Yin, Mingze Yang, Fei Wu, Yuncheng Yang, and Wenbo Hu. Sues-200: A multi-height multi-scene cross-view image benchmark across drone and satellite. *IEEE Transactions on Circuits and Systems for Video Technology*, 33(12):7667–7680, 2023. 8, 11
43. Jinliang Lin, Zhiming Luo, Dazhen Lin, Shaozi Li, and Zhun Zhong. A self-adaptive feature extraction method for aerial-view geo-localization. *IEEE Transactions on Image Processing*, 34:126–139, 2024. 10, 11
44. Tianrui Shen, Yingmei Wei, Lai Kang, Shanshan Wan, and Yee-Hong Yang. Mccg: A convnext-based multiple-classifier method for cross-view geo-localization. *IEEE Transactions on Circuits and Systems for Video Technology*, 34(3):1456–1468, 2023. 10, 11
45. Quan Chen, Tingyu Wang, Zihao Yang, Haoran Li, Rongfeng Lu, Yaoqi Sun, Bolun Zheng, and Chenggang Yan. Sdpl: Shifting-dense partition learning for uav-view geo-localization. *IEEE Transactions on Circuits and Systems for Video Technology*, 34(11):11810–11824, 2024. 10, 11
46. Haolin Du, Jingfei He, and Yuanqing Zhao. Ccr: A counterfactual causal reasoning-based method for cross-view geo-localization. *IEEE Transactions on Circuits and Systems for Video Technology*, 34(11):11630–11643, 2024. 10, 11
47. Zhongwei Chen, Zhao-Xu Yang, and Hai-Jun Rong. Multilevel embedding and alignment network with consistency and invariance learning for cross-view geo-localization. *IEEE Transactions on Geoscience and Remote Sensing*, 63:1–15, 2025. 10, 11
48. Cheng Fang, Jingchun Gao, Ping Han, Chaoyu Zhao, and Bing Gao. Scof: Supervised contrastive orthogonal fusion for robust cross-view geolocalization. *IEEE Transactions on Geoscience and Remote Sensing*, 63:1–15, 2025. 10, 11
49. Qiong Wu, Yi Wan, Zhi Zheng, Yongjun Zhang, Guangshuai Wang, and Zhenyang Zhao. Camp: A cross-view geo-localization method using contrastive attributes mining and position-aware partitioning. *IEEE Transactions on Geoscience and Remote Sensing*, 62:1–14, 2024. 9, 10, 11, 12
50. Panwang Xia, Yi Wan, Zhi Zheng, Yongjun Zhang, and Jiwei Deng. Enhancing cross-view geo-localization with domain alignment and scene consistency. *IEEE Transactions on Circuits and Systems for Video Technology*, 34(12):13271–13281, 2024. 10, 11
51. Shuyu Hu, Zelin Shi, Tong Jin, and Yunpeng Liu. Query-driven feature learning for cross-view geo-localization. *IEEE Transactions on Geoscience and Remote Sensing*, 63:1–15, 2025. 9, 10, 11
52. Xin Zhou, Xuerong Yang, and Yanchun Zhang. Cdm-net: A framework for cross-view geo-localization with multimodal data. *IEEE Transactions on Geoscience and Remote Sensing*, 63:1–16, 2025. 10, 11

53. Hongyu Zhou, Yunzhou Zhang, Tingsong Huang, Fawei Ge, Man Qi, Xichen Zhang, and Yizhong Zhang. Jrn-geo: A joint perception network based on rgb and normal images for cross-view geo-localization. In *2025 IEEE International Conference on Robotics and Automation (ICRA)*, pages 3662–3668. IEEE, 2025. [9](#), [10](#)
54. Ming Dai, Enhui Zheng, Zhenhua Feng, Lei Qi, Jiedong Zhuang, and Wankou Yang. Vision-based uav self-positioning in low-altitude urban environments. *IEEE Transactions on Image Processing*, 33:493–508, 2023. [11](#)
55. Kun Liu and Wensheng Zhang. Surfnet: A surface-aware uav–satellite geolocation framework via feature aggregation and dual positional encoding. *IEEE Transactions on Geoscience and Remote Sensing*, 64:1–15, 2026. [11](#), [12](#)